Journal of Materials Chemistry B

PAPER

Cite this: J. Mater. Chem. B, 2017, 5, 1779

In situ fabrication of Ni nanoparticles on N-doped TiO_2 nanowire arrays by nitridation of $NiTiO_3$ for highly sensitive and enzyme-free glucose sensing†

Jiangwen Xu,‡[a] Na Xu,‡[ad] Xuming Zhang,*[ac] Biao Gao,[a] Ben Zhang,[a] Xiang Peng,[c] Jijiang Fu,*[ad] Paul K. Chu[c] and Kaifu Huo[b]

Received 25th October 2016,
Accepted 1st February 2017

DOI: 10.1039/c6tb02784a

rsc.li/materials-b

A novel and simple strategy for the *in situ* fabrication of the microstructure composed of nickel (Ni) nanoparticles on nitrogen-doped TiO_2 nanowire arrays (Ni NPs/TiO_xN_y NWAs) by nitridation of $NiTiO_3$ nanowire arrays is designed and described. During nitridation, Ni is separated from $NiTiO_3$ and aggregates uniformly on the surface. The reshaped composite that is supported by the compact structure and interface of the formed NPs and remaining highly conductive TiO_xN_y NW forms a robust electrode in highly sensitive and selective non-enzymatic glucose sensing. The materials exhibit outstanding electrocatalytic activity for glucose oxidation boasting a sensitivity of 421 μA mM^{-1} cm^{-2}, a low detection limit of 0.39 μM, as well as high selectivity against interfering species such as ascorbic acid (AA), uric acid (UA) and dopamine (DA).

Introduction

Because of the variable band gaps, multiple valence states, and tunable optical and electrical properties, transition metal oxides (TMOs) such as CuO, MnO_2, Co_3O_4, and NiO have large potential in catalysis, energy storage and conservation, as well as biosensing.[1–4] The high catalytic ability of TMOs is one of their most attractive properties in non-enzymatic electrooxidation of small molecules such as glucose and H_2O_2 thereby rendering them suitable for disease diagnosis.[5,6] To boost their electrochemical performance, efforts have been made to construct nanostructured TMO with a large active surface area by hydrothermal treatment, anodization, electrochemical deposition, and the sol–gel method.[7–10] However, these nanomaterials can form close-packed structures which not only reduce the specific surface area, but also increase the contact resistance consequently leading to deteriorated stability and sensitivity. Hence, the design and fabrication of an ordered nanocomposite electrode with both the optimal mass and electron transport are crucial in order to improve the electrochemical kinetics occurring between the target molecules and the surface of the catalyst and establish conductive pathways.[11]

Among the various types of TMOs, NiO is promising as an electrocatalytic material in non-enzymatic glucose sensing as a result of the strong reversible redox couple of Ni^{3+}/Ni^{2+} in hydroxide under alkaline conditions in addition to easy fabrication and being economical and abundant.[12] Generally, the high resistance of TMOs is a common problem when they are used as electrode materials. What is more, the electrocatalytic reaction mainly relies on the surface oxide layer and the inner oxide makes limited contributions to the electrochemical reaction and aggrandizes the internal resistance. In our previous work, we synthesized a 15 nm thick $Ni(OH)_2/TiO_2$ composite film on NiTi by anodization, and in glucose oxidation, a high sensitivity of 192 μA mM^{-1} cm^{-2}, a low detection limit of 8 μM, and a broad linear range of up to 14 mM were achieved.[7] This suggests that a nanocomposite composed of an exposed TMO thin layer on a conductive support or a metal matrix with a self-formed oxide layer is desirable and could be an excellent catalyst for application in sensing. For example, Liu *et al.* synthesized a Ni NP loaded carbon nanofiber paste electrode which exhibited a sensitivity of 420 μA mM^{-1} cm^{-2}, a detection limit of 1 μM, and a linear range of 0.002–2.5 mM in non-enzymatic glucose detection.[13] Yang *et al.* prepared chitosan-reduced graphene oxide–Ni NP nanocomposite electrodes showing a wide linear range of up to 9 mM, a sensitivity up to 318.4 μA mM^{-1} cm^{-2}, as well as a detection limit of 4.1 μM.[14] Zhang *et al.* fabricated hierarchical porous core–shell Ni/NiO by a complex hydrothermal reaction, annealing, and plasma treatment and a sensitivity of

[a] The State Key Laboratory of Refractories and Metallurgy, School of Materials and Metallurgy, Wuhan University of Science and Technology, Wuhan 430081, P. R. China. E-mail: xumzhang@wust.edu.cn, fujijiang@wust.edu.cn
[b] Wuhan National Laboratory for Optoelectronics, Huazhong University of Science and Technology, Wuhan, 430074, P. R. China
[c] Department of Materials Science and Physics, City University of Hong Kong, Tat Chee Avenue, Kowloon, Hong Kong, China
[d] Institute of Biology and Medicine, Wuhan University of Science and Technology, Wuhan, 430065, P. R. China

† Electronic supplementary information (ESI) available. See DOI: 10.1039/c6tb02784a

‡ These authors contributed equally to this work.

4.49 mA mM^{-1} cm^{-2} and a detection limit of 10 μM were accomplished in glucose detection.[12]

To further boost the electrochemical performance of TMOs for sensing applications, one-dimensional (1D) nanostructured materials such as nanowires and nanotubes are desirable, because they not only reduce electron loss by confining the electron transfer direction, but also promote electrolyte transport and ion diffusion in the large space around the 1D structures.[15,16] For instance, we produced core–shell TiC/C nanowire arrays directly on Ti alloy with superior electron transport efficiency for high performance sensing applications after decoration with different active materials.[17,18] Choi *et al.* fabricated Ni modified CNT nanocomposites by atomic layer deposition (ALD) and the materials showed enhanced electrocatalytic activity and good selectivity for glucose detection.[19] Yu *et al.* prepared Ni NP loaded TiO_2 nanotube arrays by electrochemical deposition displaying high electrocatalytic activity for the oxidation of glucose.[20] However, because of the inherent drawbacks of NPs and composite electrodes, such as self-agglomeration, grain growth and structural instability, uniform and controllable immobilization of electroactive sites on 1D nanostructures with strong bonding by an economic and facile method is still challenging for an excellent electrode with a wide linear range, high sensitivity and long-term stability.

Therefore, by exploiting the advantages of Ni NPs and 1D nanostructures, we herein demonstrate a novel method to fabricate robust electrodes composed of Ni NPs grown *in situ* on N-doped TiO_2 nanowire arrays (Ni NPs/TiO_xN_y NWAs) by simple reduction of precursor $NiTiO_3$ NWAs in ammonia (NH_3) atmosphere. A phase separation mechanism was proposed in this work which overcomes the disadvantages of agglomeration of NPs and structural instability in traditional methods. Moreover, the reserved N-doped TiO_2 nanowire arrays show high conductivity in favor of electron transport.[21] The fabrication process is illustrated in Scheme 1. In this process, sodium titanate (Na_2TiO_3) NWAs are fabricated by a hydrothermal method using Ti foil in 1 M sodium hydroxide (NaOH), and nickel titanate ($NiTiO_3$) NWAs are obtained by ion exchange in a nickel acetate ($Ni(Ac)_2$) solution in a water bath. Ni is spontaneously separated from $NiTiO_3$ and NPs are formed on the surface of the remaining TiO_xN_y NWs after nitridation in an ammonia (NH_3) atmosphere. Consequently, the Ni NPs/TiO_xN_y NWAs deliver excellent performance in non-enzymatic glucose sensing because of their unique nanostructure and excellent electrocatalytic properties such as long-term stability, sensitivity, as well as selectivity.

Experimental details

Materials

The titanium foils (purity: 99.6%) were purchased from Advent Materials. Sodium hydroxide (NaOH), nickel acetate ($Ni(Ac)_2$), and hydrochloric acid (HCl) were purchased from Tianjin Chemical Company (China) and D-(+)-Glucose, L-ascorbic acid (AA), uric acid (UA) and dopamine (DA) were obtained from Sigma. All the chemicals were used as received and deionized (DI) water was used throughout the electrochemical experiments. Human blood was acquired from a local hospital.

Characterization techniques

Field-emission scanning electron microscopy (FE-SEM, FEI Nova 400 Nano, Eindhoven, the Netherlands), transmission electron microscopy (TEM, HRTEM, JEOL 2010, Tokyo, Japan), X-ray diffraction (XRD, Philips X'Pert Pro), and X-ray photoelectron spectroscopy (XPS, ESCALB MK-II,VG Instruments, London, UK) were employed to characterize the morphology, microstructure, and composition of the samples.

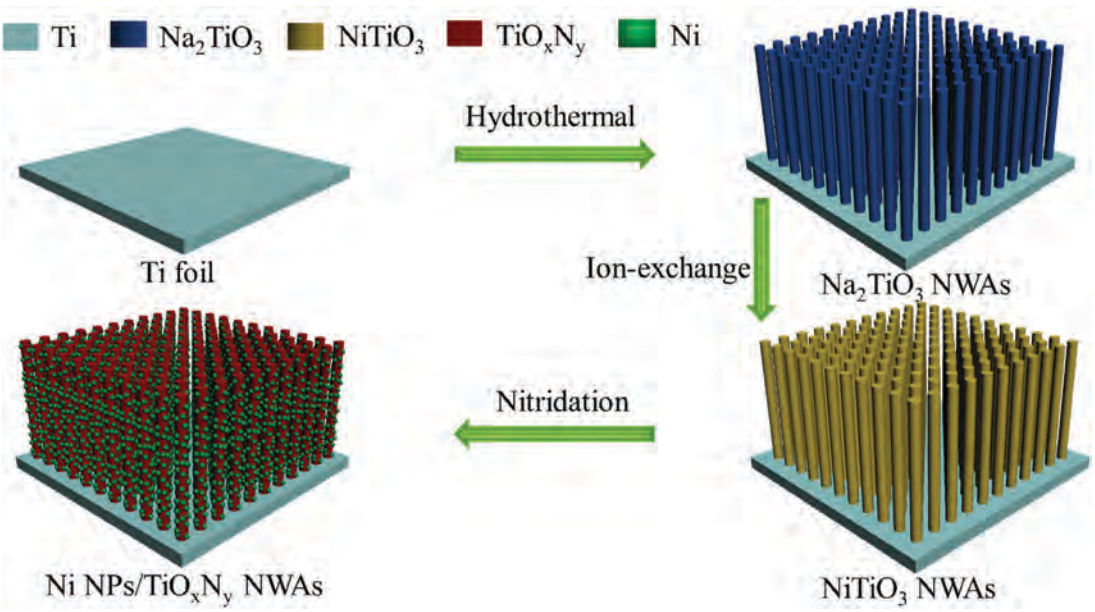

Scheme 1 Illustration of the synthesis of Ni NPs/TiO_xN_y NWAs.

Synthetic procedures

Ti foil was polished with SiC sandpaper, ultrasonically cleaned with acetone, ethanol, and DI water sequentially, and dried under flowing nitrogen at room temperature. It was then immersed in 1 M NaOH in a Teflon-lined autoclave and the sealed autoclave was heated to 210 °C and kept for 10 h to fabricate Na_2TiO_3 NWAs on the Ti foil.[22] Afterwards, the hydrothermally treated Ti foil was immersed in a 0.6 M $Ni(Ac)_2$ solution at 85 °C for 72 h to form $NiTiO_3$ NWAs by ion exchange[23] and the product was removed from the autoclave, washed with DI water for 3 min, and dried in air. The sample was further annealed in NH_3 at 500 °C for 3 h to obtain Ni NPs/TiO_xN_y NWAs. The bare TiO_xN_y NWAs were obtained by ion exchange of Na_2TiO_3 NWAs in 1 M HCl for 72 h at room temperature and a subsequent ammonia treatment.

Electrochemical measurement

Electrochemical measurement was performed on a conventional three-electrode cell with a potentiostat (CHI, Chi660e), in which the Ti foil with an exposed active area of 0.7 × 0.7 cm^2, Pt foil, and a saturated calomel electrode (SCE) served as the working electrode, counter electrode, and reference electrode, respectively. Prior to the experiment, the electrodes were activated by cyclic voltammetry (CV) at a scanning rates of 50 mV s^{-1} for 100 cycles in 1.0 M NaOH at room temperature (25 ± 2 °C).

Cyclic voltammetry (CV) was carried out under continuous stirring. The amperometric response of the Ni NPs/TiO_xN_y NWAs was recorded by successive addition of glucose to 10 ml of 1 M NaOH solution. AA, UA and DA were used as interfering species in the selectivity assessment. The amperometric response of the Ni NPs/TiO_xN_y NWAs towards real samples (human blood) was evaluated by successive addition of 100 μl of blood to 10 ml of 1 M NaOH. The original content of glucose in blood was measured using a glucometer (GM, HGM-112, Omron) for comparison. Electrochemical impedance spectroscopy (EIS) was performed in 1 M NaOH at the open-circuit potential with an AC perturbation voltage of 5 mV in the frequency range between 0.1 Hz and 100 KHz.

Results and discussion

Fig. 1a–c illustrate the morphological evolution after the hydrothermal treatment, ion exchange, and nitridation. After the hydrothermal treatment in 1 M NaOH at 210 °C for 10 h, quasi-ordered NWs with a diameter of 50–100 nm and a length of 2 micrometers are observed from the Ti foil (Fig. S1a, ESI†). After immersion in a 0.6 M $Ni(Ac)_2$ solution at 85 °C for 72 h, the structure does not change visibly (Fig. 1b). However, during annealing in NH_3 at 500 °C for 3 h (Fig. 1c), many small NPs with a diameter of about 20 nm grow uniformly on the NWs without agglomeration and this is different from the TiO_xN_y NWAs with a smooth surface (Fig. S1b, ESI†). To determine the crystallographic evolution, X-ray diffraction (XRD) patterns are

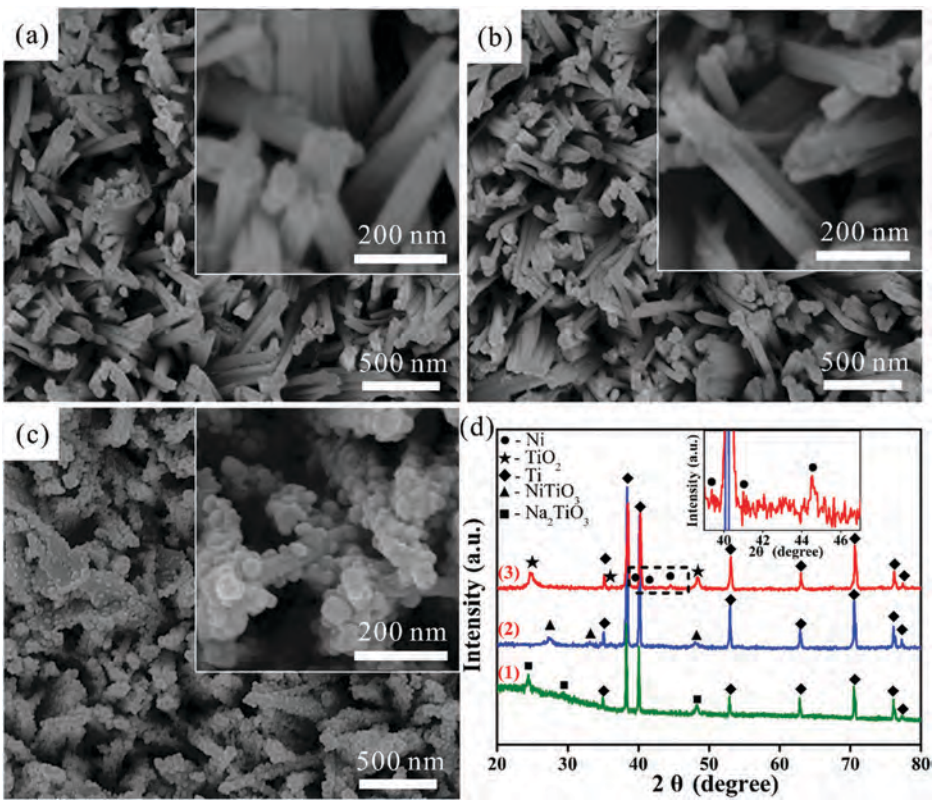

Fig. 1 SEM images of (a) Na_2TiO_3 NWAs, (b) $NiTiO_3$ NWAs, and (c) Ni NPs/TiO_xN_y NWAs; (d) the corresponding XRD patterns of (1) Na_2TiO_3 NWAs (green line), (2) $NiTiO_3$ NWAs (blue line), and (3) Ni NPs/TiO_xN_y NWAs (red line). The inset figures are the corresponding magnified images.

acquired (Fig. 1d). The XRD pattern acquired from the hydrothermal product shows strong diffraction peaks related to Na_2TiO_3 (JCPDS. No. 50-0110) in addition to the peaks from the Ti substrate (green line in Fig. 1d).[22] After ion exchange in the $Ni(Ac)_2$ solution, the characteristic diffraction peaks of Na_2TiO_3 disappear and the diffraction peaks at 28° and 33° indexed to $NiTiO_3$ emerge (JPCDS card No. 33-0960) (blue line in Fig. 1d).[8] After further nitridation, the XRD pattern (red line in Fig. 1d) shows weak metallic Ni peaks at 41.5° and 44.5° (JPCDS card No. 45-1027) in addition to the strong anatase TiO_2 peaks at 25.2° and 48° (JPCDS card No. 20-1272),[8,19] while the $NiTiO_3$ phase cannot be observed anymore. The result suggests that $NiTiO_3$ transforms into metallic Ni and anatase TiO_2 during reduction by NH_3.

Transmission electron microscopy (TEM) and energy dispersive X-ray spectroscopy (EDS) elemental mapping are performed to characterize the microstructure of the nitrided $NiTiO_3$ NWAs. The low-resolution TEM image reveals that many NPs with an approximate diameter of 20 nm are uniformly distributed on the surface of the NWs without agglomeration (Fig. S2a, ESI†). The high-resolution TEM image discloses good contact between the NW and the NP as shown in Fig. 2a and the lattice fringes show that the interplanar distance of the NW is 0.35 nm, which is indicative of (101) anatase TiO_2.[24] Fig. 2b shows a crystal plane spacing of 0.2 nm between two neighboring fringes in the NP corresponding to the *d*-spacing of the (111) plane of metallic Ni.[19] As shown in Fig. S2b (ESI†), the HR-TEM image of Ni NPs/TiO_xN_y NWAs indicates that Ni NPs are wrapped up by a thin amorphous NiO layer after exposing to air for several days. The EDS maps in Fig. 2c show uniform distributions of Ti, O and N in the NW except the enriched region of Ni. The results indicate the segregation of Ni from $NiTiO_3$ after nitridation, which is consistent with XRD and TEM results. X-ray photoelectron spectroscopy (XPS) is carried out to investigate the chemical states of Ni 2p, Ti 2p, O 1s, and N 1s. The survey XPS spectra of the nitrided product are presented in Fig. S2c (ESI†). C 1s (284.6 eV) may stem from the contamination from the chamber. Fig. 3a shows the fine Ni $2p_{3/2}$ spectrum which can be fitted with three sub-peaks at 852.3 eV, 855.1 eV, and 861 eV corresponding to metallic Ni, NiO, and a satellite peak.[25–27] The oxidized state stems from the oxide layer on the surface of the Ni NPs (Fig. S2b, ESI†). The Ti 2p spectrum in Fig. 3b can be deconvoluted into two oxidation states: Ti^{4+} in TiO_2 (Ti $2p_{3/2}$, 458.5 eV; Ti $2p_{1/2}$, 464.3 eV) and the suboxide state of Ti in TiO_xN_y (Ti $2p_{3/2}$, 456.9 eV; Ti $2p_{1/2}$, 462.5 eV), respectively. It has been reported that the thermal treatment of the stoichiometric TiO_2 in NH_3 could result in the shifting of Ti $2p_{3/2}$ towards low binding energy due to the effects of both nitrogen doping and oxygen vacancy formation.[28] The O1s peak can be fitted with Ti–O (530.2 eV), absorbed O_2/H_2O (531.2 eV), and TiO_xN_y (533.8 eV) and the fitted N 1s ones at 396.1 eV and 398 eV obtained from TiO_xN_y are characteristic of N^{3+} in TiN and the Ti–N–O or Ti–O–N oxynitride, respectively.[28–30] The results clearly indicate the co-existence of metallic Ni NPs with a thin NiO coating and N-doped TiO_2 after nitridation of $NiTiO_3$ NWAs. The atomic ratio of N/Ti in the remaining NWs is as large as 0.5 suggesting a large concentration of doped nitrogen which benefits the conductivity of NWs (Table S1, ESI†).[31]

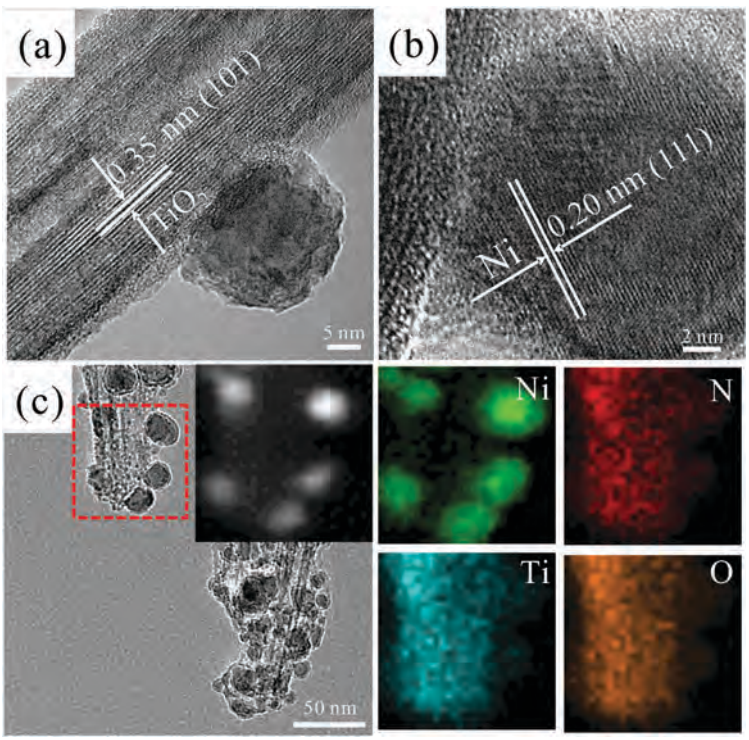

Fig. 2 (a) and (b) HR-TEM images of Ni NPs/TiO_xN_y NWs. (c) TEM image and the corresponding elemental maps of N, O, Ti and Ni. The inset figure in (c) was corresponding dark field image of dotted square.

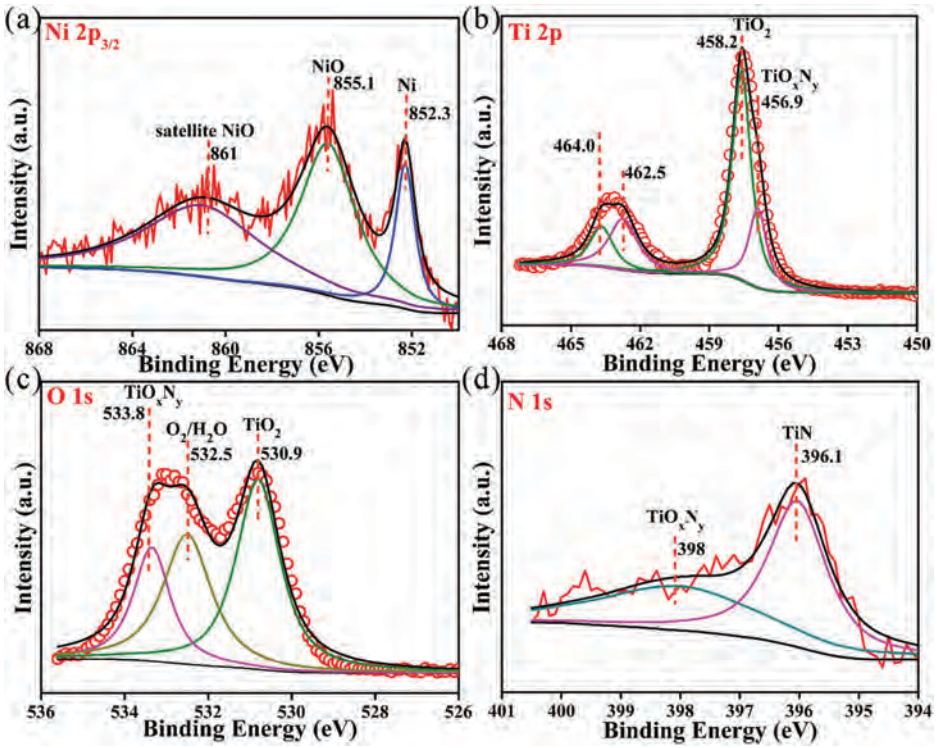

Fig. 3 Fine XPS spectra of (a) Ni 2p3/2, (b) Ti 2p, (c) O 1s, and (d) N 1s acquired from the Ni NPs/TiO_xN_y NWAs.

The electrochemical behavior of the Ni NP/TiO_xN_y NWA electrode is investigated at room temperature using a three-electrode configuration. 1 M NaOH solution is used as the electrolyte because of the smallest peak-to-peak potential separation (ΔE_p) (Fig. S3, ESI†). Fig. 4a shows the CV curves of the Na_2TiO_3 NWAs, ion-exchanged $NiTiO_3$ NWAs, and Ni NPs/TiO_xN_y NWAs at a scanning rate of 50 mV s^{-1}. No obvious peaks are observed from TiO_xN_y NWAs and $NiTiO_3$ NWAs, but a pair of well-defined peaks corresponding to the Ni^{2+}/Ni^{3+} redox couple can be observed from Ni NPs/TiO_xN_y NWAs due to the following reactions:[32]

$$Ni + 2OH^- \rightarrow Ni(OH)_2 + 2e^- \quad (1)$$

$$Ni(OH)_2 + OH^- \leftrightarrow NiO(OH) + H_2O + e^- \quad (2)$$

Fig. 4b shows the CV profile of the Ni NPs/TiO_xN_y NWAs at different scanning rates between 5 and 300 mV s^{-1}. The redox couple with a peak-to-peak potential separation (ΔE_p) increases gradually with scanning rates and both the anodic and cathodic peak currents bear a linear relationship with the square root of the scanning rate (inset image in Fig. 4b), indicating a typical diffusion-controlled electrochemical process which is sensitive to the glucose concentration boding well for quantitative analysis. Electrochemical impedance spectroscopy (EIS) is employed to investigate the electron transfer resistance of these electrodes. As shown in Fig. 4c, the Nyquist plots have been fitted by an equivalent circuit (inset image) in which R_s is the bulk resistance of the electrochemical system, R_{ct} is the faradic charge transfer resistance obtained from the diameter of the semicircle, and W is the Warburg impedance. The TiO_xN_y NWA electrode exhibits a much smaller R_{ct} (29.7 Ω) than that of the $NiTiO_3$ NWA electrode (red) of 18 kΩ due to N-doping. And the R_{ct} of Ni NPs/TiO_xN_y NWAs is further reduced to 1.6 Ω attributable to the metallic Ni species generated *in situ* along the walls of the NWAs.

The electrocatalytic properties of the Ni NPs/TiO_xN_y NWAs are evaluated by CV at a scanning rate of 50 mV s^{-1} in 1 M NaOH with different glucose concentrations between 0 and 10 mM. As shown in Fig. 4d, the anodic peak current increases with glucose concentration on account of the catalytic Ni^{3+} species on the Ni NPs according to the following irreversible reaction:[33,34]

$$NiO(OH) + glucose \rightarrow Ni(OH)_2 + glucolactone \quad (3)$$

When glucose diffuses into the electrode surface, it is rapidly oxidized by Ni^{3+} which is reduced to Ni^{2+}. At the anodic potential, Ni^{2+} is oxidized back to Ni^{3+}. As the amount of glucose is increased, more glucose molecules are involved in the catalytic reaction and oxidized by the diffusion-controlled process resulting in a fast increase in the anodic peak current. The applied potential affects the response of the electrochemical biosensor because the reaction involves the oxidation of water molecules. As shown in Fig. S4 (ESI†), the optimal applied potential is 0.37 V (*vs.* SCE) based on the better amperometric response.

Fig. 5a shows the amperometric response of the Ni NP/TiO_xN_y NWA electrode during the successive addition of glucose at a potential of 0.37 V (*vs.* SCE) in 1 M NaOH under stirring. It shows a sensitive response even when the glucose concentration is 1 μM and a fast response reaching the steady state within 2.8 s is observed (inset in Fig. 5a). As shown in Fig. 5b, the calibration curve exhibits two linear ranges from 1 μM to 1 mM with a

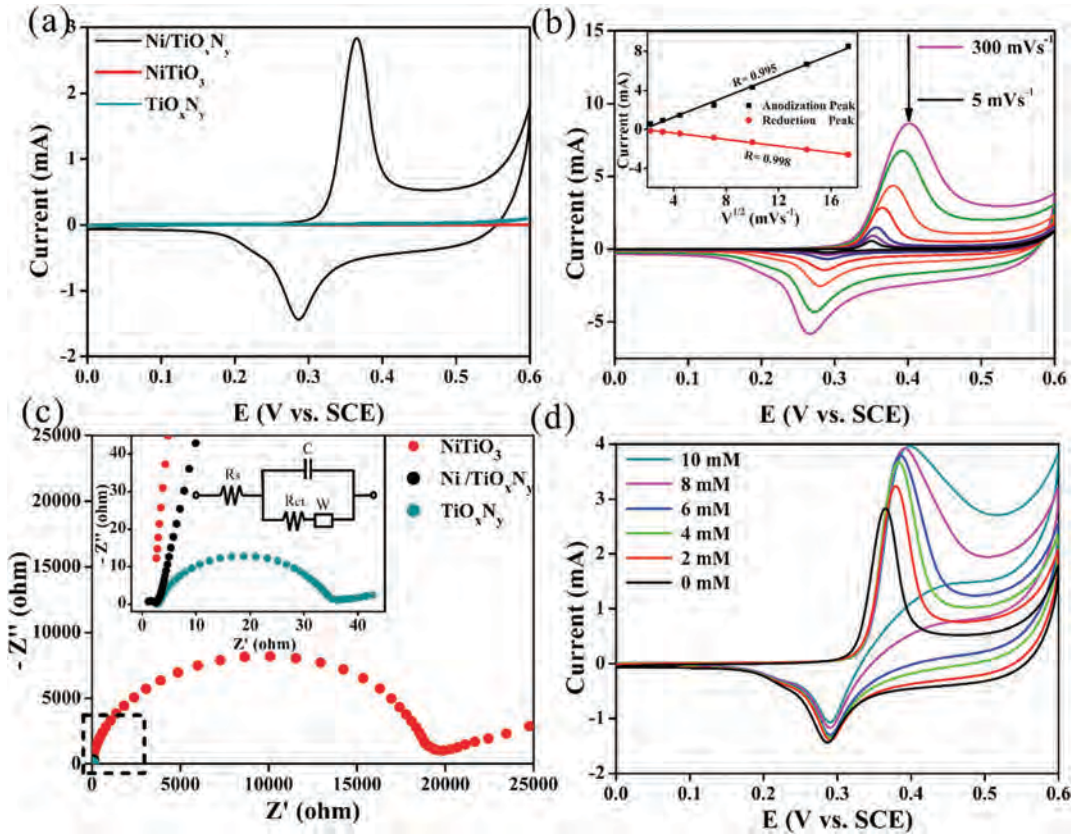

Fig. 4 (a) CV of the $NiTiO_3$ NWA electrode (red), the TiO_xN_y NWA electrode (dark cyan), and the Ni NP/TiO_xN_y NWA electrode (black); (b) CVs of the Ni NP/TiO_xN_y NWA electrode at different scanning rates between 5 and 300 mV s^{-1} with the inset showing a linear dependence between the anodic and cathodic peak currents and the square root of the scanning rate; (c) Nyquist plots of the $NiTiO_3$ NWA electrode (red), the TiO_xN_y NWAs electrode (blue), and the Ni NP/TiO_xN_y NWA electrode (black), the inset figure is the equivalent circuit model; (d) CVs of the Ni NP/TiO_xN_y NWA electrode with increasing concentrations of glucose from 0 to 10 mM at a scanning rate of 50 mV s^{-1}. The electrolyte used in CV and EIS is 1 M NaOH.

sensitivity of 421 μA mM^{-1} cm^{-2} (correction coefficient R = 0.996) and 1 to 7 mM with a sensitivity of 228.92 μA mM^{-1} cm^{-2} (correction coefficient R = 0.997). The detection limit is found to be 0.39 μM at a signal-to-noise ratio of 3, which is much smaller than those obtained from other Ni-based non-enzymatic glucose sensors (Table 1) such as the 3D Ni-graphene core–shell electrodes,[35] Ni/Al hydroxide nanosheets,[36] Ni-decorated TiO_2 nanotube arrays on Ti foils,[37] chitosan-reduced graphene oxide–Ni NPs nanocomposites,[14] $CoNiO_2$ NWs on TiN–TiO_xN_y flexible electrodes,[38] Ni NP loaded CFP (carbon nanofiber paste) electrodes,[13] and Ni NWA modified glassy carbon electrodes.[39] The excellent electrocatalytic performance results from the activated NiO thin layer on the Ni NPs and fast electron transfer between the Ni NPs and the underlying current collector. It is also noted that the fabrication method described reduces electrical signal loss from the electroactive sites to the current collector.

Ascorbic acid (AA), uric acid (UA) and dopamine (DA), three common interfering species co-existing with glucose in blood, can be simultaneously oxidized at low applied potential on the sensor electrode compromising the accuracy.[40,41] Considering that the actual concentration of glucose in blood is much larger than those of AA, UA and DA, the amperometric response of the Ni NP/TiO_xN_y NWA electrode during successive addition of 5 mM glucose, 0.3 mM AA, 0.3 mM UA and 0.3 mM DA at a potential of 0.37 V (*vs.* SCE) in 1.0 M NaOH is monitored (Fig. 5c). Insignificant responses of 1.6%, 0.9% and 4.7% are observed from AA, UA, and DA, respectively, in the presence of 5 mM glucose. The reliability of the Ni NPs/TiO_xN_y NWAs in routine analysis is evaluated on real blood samples. As shown in Fig. 5d, at the optimal applied potential of 0.37 V (*vs.* SCE), 0.1 mL of fresh human blood is added successively to 10 ml of 1 M NaOH under stirring. After calculating the current response (see the ESI†), the glucose content in blood is determined to be 5.89 mM which is in good agreement with that measured by a commercial glucose meter (5.7 mM) (inset image in Fig. 5d) showing a mere difference of 3.3%.

The reproducibility and long-term stability of the Ni NP/TiO_xN_y NWA electrode is evaluated by measuring the anodic peak current of CV curves at a scanning rate of 50 mV s^{-1} in 1 M NaOH. The average anodic peak current of four different electrodes is 2.87 ± 0.07 mA demonstrating good repeatability of the fabrication process (Fig. S5a, ESI†). After storing for 30 days in air (Fig. S5b, ESI†), the Ni NP/TiO_xN_y NWA electrode showing 2% fluctuation in the current *versus* initial anodic peak current is observed and good stability is confirmed. The morphology of the Ni NP/TiO_xN_y NWA electrode after 30 days of storage

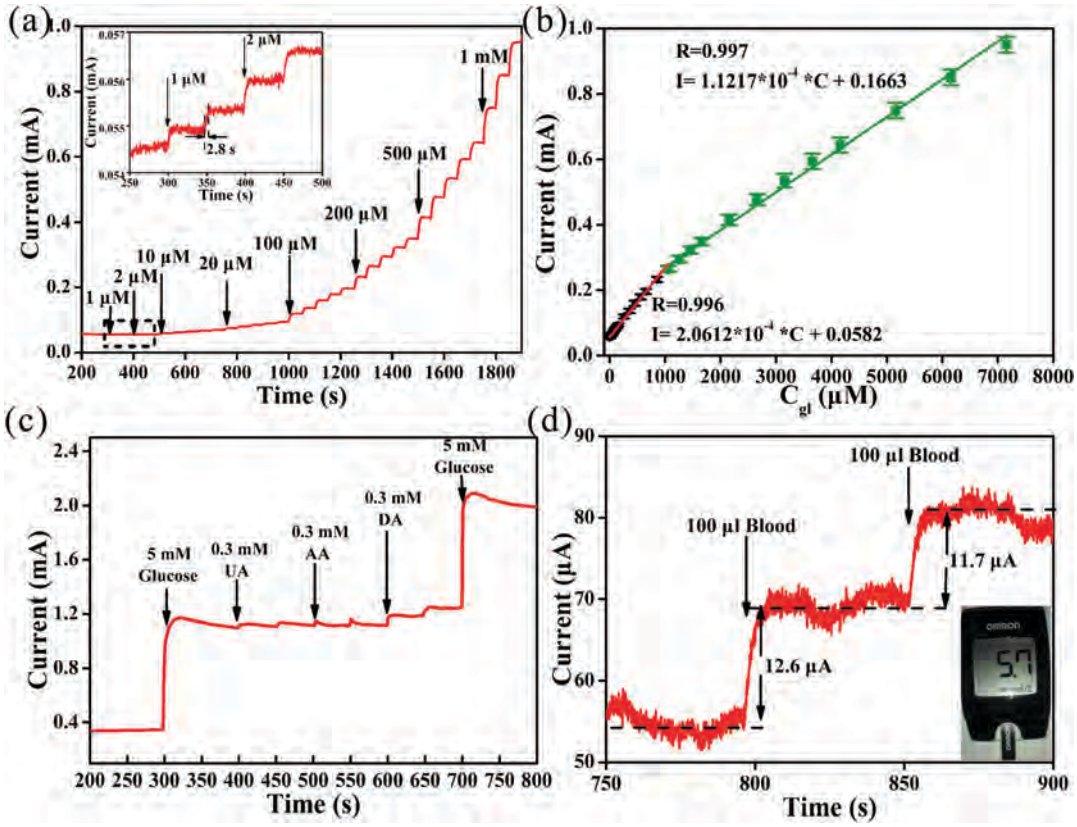

Fig. 5 (a) Amperometric response of the Ni NPs/TiO_xN_y NWAs during successive addition of glucose under stirring, the inset figure is the enlargement of the dotted square; (b) the corresponding calibration curve for the glucose concentration; (c) interference assessment of the Ni NPs/TiO_xN_y NWAs during the successive addition of 5 mM glucose, 0.3 mM AA (twice), 0.3 mM UA (twice), 0.3 mM DA (twice) and 5 mM glucose; (d) amperometric response of the Ni NPs/TiO_xN_y NWAs during the successive addition of fresh blood under stirring with the inset picture showing the determination of the same sample using a commercial glucose meter (OMRON GM). The electrolyte is 1 M NaOH and the applied potential is 0.37 V (*versus* SCE).

Table 1 Comparison of the electrochemical performance of different Ni-based non-enzymatic glucose biosensors

Electrode	Linear range (mM)	Detection limit (μM)	Sensitivity (μA mM^{-1} cm^{-2})	Ref.
Ni NPs/TiO_xN_y NWAs	0.001–1 1–7.1	0.39	421 229	This work
3D Ni–graphene core–shell	1–10	N/A	400	35
Ni/Al hydroxide nanosheets	0.005–10.0	5	24.45	36
Ti/TiO_2 nanotube arrays/Ni	0.1–1.7	4	200	37
CS-RGO[a]–Ni NPs	Up to 9	4.1	318.4	14
$CoNiO_2$/TiN–TiO_xN_y	N/A	0.1	N/A	38
Ni-CFP[b]	0.002–2.5	1	420	13
Ni NWAs/GCE[c]	0.5–7	1	1043	39

[a] CS-RGO, chitosan-reduced graphene oxide. [b] CFP, carbon nanofiber paste electrode. [c] GCE, glassy carbon electrode.

characterized by the FE-SEM image shows no obvious changes suggesting good structural stability as well (Fig. S5c, ESI†).

Conclusion

Ni NPs prepared *in situ* on conductive TiO_xN_y NWAs have excellent non-enzymatic glucose sensing capability. Nitridation of $NiTiO_3$ NWAs separates Ni NPs from NWs and forms the TiO_xN_y NWs at the same time. The Ni NPs/TiO_xN_y NWAs deliver good electrocatalytic performance in glucose sensing including a high sensitivity of 421 μA mM^{-1} cm^{-2} and a low detection limit of 0.39 μM and excellent selectivity. The excellent properties stem from fast electron transfer between the surface oxide on the Ni NPs and the underlying electrode supported by conductive TiO_xN_y NWs and the compact interface between them. The efficient and economical fabrication method which is applicable to other transition metal/oxide heterostructures has large potential in catalysis as well as energy storage and conversion.

Acknowledgements

This work was financially supported by the National Natural Science Foundation of China (51572100, 51504171, 31500783, 3144004, 81571816), the Project of Natural Science Foundation of Hubei Province (2015CFA116), the Young Science Foundation of The State Key Laboratory of Refractories and Metallurgy of Wuhan University of Science and Technology (2016QN08), and the City University of Hong Kong Applied Research Grant (ARG) No. 9667122 and Strategic Research Grant (SRG) No. 7004644.

Notes and references

1 Y. W. Hsu, T. K. Hsu, C. L. Sun, Y. T. Nien, N. W. Pu and M. D. Ger, *Electrochim. Acta*, 2012, **82**, 152–157.
2 L. Han, C. Shao, B. Liang and A. Liu, *ACS Appl. Mater. Interfaces*, 2016, **8**, 13768–13776.
3 J. Mu, L. Zhang, M. Zhao and Y. Wang, *ACS Appl. Mater. Interfaces*, 2014, **6**, 7090–7098.
4 X. Zhuang, C. Tian, F. Luan, X. Wu and L. Chen, *RSC Adv.*, 2016, **6**, 92541–92546.
5 H. Liu, X. Wu, B. Yang, Z. Li, L. Lei and X. Zhang, *Electrochim. Acta*, 2015, **174**, 745–752.
6 M. Mahmoudian, W. Basirun, P. M. Woi, M. Sookhakian, R. Yousefi, H. Ghadimi and Y. Alias, *Mater. Sci. Eng., C*, 2016, **59**, 500–508.
7 A. Gao, X. Zhang, X. Peng, H. Wu, L. Bai, W. Jin, G. Wu, R. Hang and P. K. Chu, *Sens. Actuators, B*, 2016, **232**, 150–157.
8 K. Huo, Y. Li, R. Chen, B. Gao, C. Peng, W. Zhang, L. Hu, X. Zhang and P. K. Chu, *ChemPlusChem*, 2015, **80**, 576–582.
9 H. Yi, X. Chen, H. Wang and X. Wang, *Electrochim. Acta*, 2014, **116**, 372–378.
10 D. P. Debecker and P. H. Mutin, *Chem. Soc. Rev.*, 2012, **41**, 3624–3650.
11 M. Li, C. Han, Y. Zhang, X. Bo and L. Guo, *Anal. Chim. Acta*, 2015, **861**, 25–35.
12 C. Zhang, L. Qian, K. Zhang, S. Yuan, J. Xiao and S. Wang, *J. Mater. Chem. A*, 2015, **3**, 10519–10525.
13 Y. Liu, H. Teng, H. Hou and T. You, *Biosens. Bioelectron.*, 2009, **24**, 3329–3334.
14 J. Yang, J. Yu, J. Rudi Strickler, W. Chang and S. Gunasekaran, *Biosens. Bioelectron.*, 2013, **47**, 530–538.
15 X. Huang and Y. Choi, *Sens. Actuators, B*, 2007, **122**, 659–671.
16 A. Liu, *Biosens. Bioelectron.*, 2008, **24**, 167–177.
17 X. Zhang, K. Huo, H. Wang, B. Gao, J. Fu, T.-F. Hung and P. K. Chu, *ACS Appl. Mater. Interfaces*, 2012, **4**, 1037–1042.
18 X. Zhang, L. Li, X. Peng, R. Chen, K. Huo and P. K. Chu, *Electrochim. Acta*, 2013, **108**, 491–496.
19 T. Choi, S. H. Kim, C. W. Lee, H. Kim, S.-K. Choi, S.-H. Kim, E. Kim, J. Park and H. Kim, *Biosens. Bioelectron.*, 2015, **63**, 325–330.
20 S. Yu, X. Peng, G. Cao, M. Zhou, L. Qiao, J. Yao and H. He, *Electrochim. Acta*, 2012, **76**, 512–517.
21 I. Milošv, H.-H. Strehblow, B. Navinšek and M. Metikoš-Huković, *Surf. Interface Anal.*, 1995, **23**, 529–539.
22 J.-Y. Liao, B.-X. Lei, H.-Y. Chen, D.-B. Kuang and C.-Y. Su, *Energy Environ. Sci.*, 2012, **5**, 5750–5757.
23 N. Li, L. Zhang, Y. Chen, M. Fang, J. Zhang and H. Wang, *Adv. Funct. Mater.*, 2012, **22**, 835–841.
24 Q. Zhang, Y. Wang, Y. Wang, A. M. Al-Enizi, A. A. Elzatahry and G. Zheng, *J. Mater. Chem. A*, 2016, **4**, 5713–5718.
25 H. Ali-Löytty, M. W. Louie, M. R. Singh, L. Li, H. G. Sanchez Casalongue, H. Ogasawara, E. J. Crumlin, Z. Liu, A. T. Bell and A. Nilsson, *J. Phys. Chem. C*, 2016, **120**, 2247–2253.
26 A. A. Ensafi, N. Ahmadi and B. Rezaei, *Sens. Actuators, B*, 2017, **239**, 807–815.
27 P. Veerakumar, S. Chen, R. Madhu, V. Veeramani, C.-T. Hung and S. Liu, *ACS Appl. Mater. Interfaces*, 2015, **7**, 24810–24821.
28 J. Wang, D. N. Tafen, J. P. Lewis, Z. Hong, A. Manivannan, M. Zhi, M. Li and N. Wu, *J. Am. Chem. Soc.*, 2009, **131**, 12290–12297.
29 B. Avasarala and P. Haldar, *Electrochim. Acta*, 2010, **55**, 9024–9034.
30 Y. Chen, X. Cao, B. Lin and B. Gao, *Appl. Surf. Sci.*, 2013, **264**, 845–852.
31 G. Greczynski and L. Hultman, *Appl. Surf. Sci.*, 2016, **387**, 294–300.
32 S. Fu, G. Fan, L. Yang and F. Li, *Electrochim. Acta*, 2015, **152**, 146–154.
33 Y. Gao, L. Wang, W. Zhang, X. Yang, Y. Ma, J. Shao and Y. Li, *Electrochim. Acta*, 2016, **201**, 260–267.
34 G. Wang, X. Lu, T. Zhai, Y. Ling, H. Wang, Y. Tong and Y. Li, *Nanoscale*, 2012, **4**, 3123–3127.
35 X. Xiao, J. R. Michael, T. Beechem, A. McDonald, M. Rodriguez, M. T. Brumbach, T. N. Lambert, C. M. Washburn, J. Wang and S. M. Brozik, *J. Mater. Chem.*, 2012, **22**, 23749–23754.
36 X. Li, J. Liu, X. Ji, J. Jiang, R. Ding, Y. Hu, A. Hu and X. Huang, *Sens. Actuators, B*, 2010, **147**, 241–247.
37 C. Wang, L. Yin, L. Zhang and R. Gao, *J. Phys. Chem. C*, 2010, **114**, 4408–4413.
38 Z. Peng, D. Jia, J. Tang, Y. Wang, Y. Wang, L. Zhang and G. Zheng, *J. Mater. Chem. A*, 2014, **2**, 10904–10909.
39 L. Lu, L. Zhang, F. Qu, H. Lu, X. Zhang, Z. Wu, S. Huan, Q. Wang, G. Shen and R. Yu, *Biosens. Bioelectron.*, 2009, **25**, 218–223.
40 Y. Yu, M. Guo, M. Yuan, W. Liu and J. Hu, *Biosens. Bioelectron.*, 2016, **77**, 215–219.
41 M. Arvand and S. Tajyani, *RSC Adv.*, 2015, **5**, 7222–7231.